Theoretical Raman spectrum and anharmonicity of tetrahedral OH defects in hydrous forsterite

Etienne Balan, Marc Blanchard, Michele Lazzeri, Jannick Ingrin

Theoretical Raman spectrum and anharmonicity of tetrahedral OH defects in hydrous forsterite

Etienne Balan[1], Marc Blanchard[1], Michele Lazzeri[1], Jannick Ingrin[2]

[1] Institut de Minéralogie, de Physique des Matériaux, et de Cosmochimie (IMPMC), Sorbonne Universités, UPMC Univ Paris 06, UMR CNRS 7590, Muséum National d'Histoire Naturelle, UMR IRD 206, 4 place Jussieu, F-75005 Paris, France

[2] UMET, UMR CNRS 8207, Université de Lille1, Bât. C6, 59655 Villeneuve d'Ascq, France

Corresponding author:

Prof. Etienne Balan

Institut de Minéralogie, de Physique des Matériaux, et de Cosmochimie (IMPMC), Sorbonne Universités, UPMC Univ Paris 06, UMR CNRS 7590, Muséum National d'Histoire Naturelle, UMR IRD 206, 4 place Jussieu, F-75005 Paris, France

Email: Etienne.Balan@impmc.upmc.fr

Abstract: Substitutional mechanisms involving hydrogen incorporation at vacant tetrahedral sites play a major role in water incorporation in olivine. IR absorption spectra of hydrous forsterite samples usually display a cluster of narrow and weakly anharmonic OH stretching bands at wavenumbers above 3500 cm^{-1}. A broader absorption band displaying pronounced temperature-dependent shift and broadening is often superimposed to this diagnostic spectrum and was tentatively assigned to interstitial OH groups. A less frequently observed band with similar temperature-dependent characteristics is related to a coupled incorporation of hydrogen and boron at the tetrahedral site. Here, we re-examine these interpretations by computing the theoretical Raman spectrum and investigating the local vibrational properties of OH groups at the tetrahedral site of forsterite. The present results show that the two anharmonic bands are both ascribed to the protonated O2 site in the clumped $(B,H)_{Si}^{x}$ and the $(4H)_{Si}^{x}$ defects. The peculiar orientation of the corresponding OH groups does not allow H-bond sharing and leads to efficient vibrational phase relaxation of the stretching mode through a hindered rotational mode coupled to the vibrational density of states of the host. The occurrence of interstitial OH groups previously proposed to interpret specific anharmonic bands of the forsterite IR spectrum is highly challenged by this new explanation. These results confirm that at high pressure and high temperature, hydrogen incorporation in forsterite is essentially dominated by $(4H)_{Si}^{x}$ defects.

Key-words: forsterite; OH defects; IR spectroscopy; Raman spectroscopy; ab initio calculations; anharmonicity.

1. Introduction

Olivine, $(Mg,Fe)_2SiO_4$, is able to incorporate minor amounts of hydrogen as OH-bearing defects in its crystal structure (Beran & Zemman, 1969; Wilkins & Sabine, 1973; Beran & Putnis, 1983). As it is the most abundant rock-forming silicate in the upper mantle, these defects are expected to significantly contribute to the global budget of water in Earth (*e.g.*, Bell & Rossman, 1992; Bolfan-Casanova, 2005; Demouchy & Bolfan-Casanova, 2016). The related modifications of the mechanisms of plastic crystal deformation might also play an important role in plate tectonics and mantle dynamics (*e.g.*, Chopra & Paterson, 1984; Mackwell *et al*., 1985; Mei *et al*., 2000; Demouchy *et al*., 2012; Tasaka *et al*., 2015). Accordingly, the hydrogen solubility in olivine has been investigated as a function of a number of thermodynamic parameters relevant to mantle conditions (typically T=1700 K and P=10 GPa), including temperature, pressure, water activity, silica activity, and oxygen fugacity (e.g. Bai & Kohlstedt, 1993; Mosenfelder *et al*., 2006; Smyth *et al*., 2006; Grant *et al*., 2007; Withers *et al*., 2012; Férot & Bolfan-Casanova, 2012). However, the variability of incorporation mechanisms and location of OH groups in the olivine structure as revealed by the infrared spectrum of natural samples (Libowitzky & Beran, 1995; Matsyuk & Langer, 2004; Koch-Muller *et al*., 2006; Beran & Libowitzky, 2006; Matveev & Stachel, 2009; Gose *et al*., 2010) is still poorly understood.

Thermodynamic laws inferred from early measurements of water solubility in olivine were consistent with an incorporation mechanism involving an isovalent substitution of two protons for a divalent magnesium ion (*e.g.*, Kohlstedt *et al*., 1996), a model theoretically supported by the easier formation of vacancies at Mg sites than at Si sites (Walker *et al*., 2006). However, a dependence of the mechanism of hydrogen incorporation on Si and Mg

activity conditions was revealed by infrared spectroscopic observations performed on synthetic and natural olivine (Matveev *et al*., 2001; 2005) as well as on synthetic forsterite (the Mg end-member of olivine) samples (Lemaire *et al*., 2004; Berry *et al*., 2005), questioning the pertinence of the Mg-vacancy model in forsterite and olivine. The relations between the infrared spectrum and the Si and Mg activity conditions, together with the theoretical modeling of the infrared spectroscopic properties of OH defects in forsterite (Balan *et al*., 2011; Umemoto *et al*., 2011), consistently point to a dominant incorporation mechanism involving a $(4H)^{x}_{Si}$ defect, i.e. the isovalent substitution of four protons for a tetravalent silicon ion at tetrahedral sites. This mechanism leads to infrared absorption bands typically observed at frequencies above 3400 cm^{-1}; whereas protonated Mg vacancies lead to bands observed between 3100 and 3200 cm^{-1}. Similar high frequency bands are observed in the Raman spectra of synthetic hydrous forsterite samples (Hushur *et al*., 2009; Bolfan-Casanova *et al*., 2014). A preferential protonation of Si vacancies in forsterite has also been recently inferred by an NMR study combining the measurement and a theoretical modeling of chemical shift and dipolar coupling parameters (Xue *et al*., 2016). Finally, a number of absorption bands have been related to the interaction of OH bearing defects and other chemical elements in natural olivine samples and their synthetic counterparts (*e.g*., Berry *et al*., 2005, 2007; Walker *et al*., 2007; Crépisson *et al*., 2014a; Blanchard *et al*., 2016). The extrapolation of spectroscopic observations made at ambient conditions to temperatures relevant to the Earth upper mantle was however questioned by the in-situ study of Yang & Keppler (2011) who reported the infrared spectrum of hydrated San Carlos olivine recorded up to 1100 °C.

Further information on the OH defects in forsterite was obtained by studying the anharmonic behaviour of OH stretching vibrational modes, through the low-temperature dependence of its infrared absorption spectrum (Ingrin *et al*., 2013). Most of the observed

125 bands previously ascribed to OH incorporated at tetrahedral or octahedral sites displayed a
126 moderately anharmonic behaviour, slightly stronger for the more effectively H-bonded OH
127 groups at octahedral sites. In contrast, a stronger anharmonicity was inferred for two bands
128 (referred to as band 3a and band 8a; Fig. 1a) observed at high frequencies in the investigated
129 sample (3550 and 3598 cm^{-1} at room temperature for bands 3a and 8a, respectively) and
130 displaying marked temperature-dependent frequency shifts and broadenings (Fig. 1). Such
131 anomalous behaviour, distinct from that of the bands ascribed to substitutional OH groups,
132 was interpreted in Balan *et al*. (2014) using the Persson & Ryberg formalism (Persson &
133 Ryberg, 1985a,b): the anharmonic behavior is related to the indirect coupling of the high-
134 frequency vibrational stretching mode to the vibrational density of states (phonon bath) of the
135 crystalline host via a specific low-frequency vibrational mode, referred to as exchange mode.
136 A structural model corresponding to band 3a at 3550 cm^{-1} was proposed in terms of interstitial
137 OH groups. Occurrence of interstitial OH groups in olivine has been previously proposed by
138 Bai and Kohlstedt (1993). Interstitial OH groups are indeed expected to be weakly H-bonded,
139 consistent with a relatively high vibrational frequency, and significantly coupled to specific
140 low-energy vibrations leading to a strong anharmonic behaviour. A more recent spectroscopic
141 study of natural and synthetic samples revealed that the band 8a is related to a coupled
142 incorporation of hydrogen and boron at the tetrahedral site of forsterite (Ingrin *et al*., 2014). In
143 this $(H,B)_{Si}^{x}$ defect, referred to as B_H_1 defect (Ingrin *et al*., 2014), the BO_3 group occupies
144 one face of the tetrahedron, delimited by the O1 and the two symmetric O3 oxygen atoms;
145 whereas the H atom is bonded to the opposite O2 atom and points toward the exterior of the
146 tetrahedron. However, the origin of the anharmonic character of the corresponding stretching
147 band was still unclear. It became also apparent that only three of the four bands predicted for
148 the most stable configuration of protonated Si vacancies $(4H)_{Si}^{x}$, referred to as Si_3 defect
149 (Balan *et al*., 2011) were observed in the low temperature spectra. The band related to the

150 protonation of the O2 atom was systematically lacking. This set of observations thus calls for
151 an in-depth re-examination of the peculiarity of the proton environment at the O2 site in
152 forsterite and related anharmonic behaviour.
153 In the present study, we report a theoretical analysis of the energetic landscape
154 controlling the proton dynamics at the tetrahedral sites of forsterite. We also compute the
155 Raman intensity of the OH-stretching bands related to the Si_3 defect, to bring additional
156 constraints for the interpretation of the measured spectra (Hushur *et al*., 2009, Bolfan-
157 Casanova *et al*., 2014). The obtained results make it possible to reconcile different
158 experimental observations and further support a dominant mechanism of water incorporation
159 in forsterite as OH defects associated to vacant tetrahedral sites.
160

161 ## 2. Theoretical methods

162

163 The energy landscape and theoretical spectroscopic properties of the defects are
164 obtained from first-principles calculations based on density functional theory (DFT),
165 that is by solving the equation of quantum mechanics (within certain approximations)
166 without using ad-hoc phenomenological parameterization. This approach is commonly
167 considered as predictive for the systems under consideration. The theoretical approach
168 and convergence parameters are the same as in Balan *et al*. (2011). To summarize,
169 calculations were performed using the generalized gradient approximation (GGA) to the
170 exchange-correlation functional (Perdew *et al*., 1996) with the PWscf code of the Quantum
171 Espresso package (Gianozzi *et al*., 2009; http://www.quantum-espresso.org). Periodic models
172 of OH-bearing forsterite were built by inserting one defect in a 2x1x2 supercell (112 atoms)
173 of forsterite (theoretical primitive cell-parameters: a = 4.78 Å, b = 10.28 Å, and c = 6.01 Å).
174 The equilibrium positions were determined at constant volume by minimizing the forces on

atoms to less than 10^{-5} Ry/a.u. (1 Ry=13.6057 eV). The harmonic vibrational modes were calculated at the Brillouin zone center (**Γ** point), using the linear response theory (Baroni *et al*., 2001) as implemented in the PHonon code (Gianozzi *et al*., 2009; http://www.quantum-espresso.org). Potential energy surfaces related to selected hydrogen atoms were obtained by calculating the total energy of the system for a series of finite displacements of the hydrogen from its equilibrium position. The Raman spectrum of the Si_3 defect was computed using the vibrational modes previously determined in Balan *et al*. (2011) and the Raman tensors obtained using the second-order response to density functional theory as exposed in Lazzeri and Mauri (2003).

3. Results and discussion

3.1 Anharmonic OH-stretching bands in forsterite : Reappraisal of experimental data

As previously exposed in Ingrin *et al*. (2013), two OH-stretching bands (bands 3a and 8a, Fig. 1a) observed in hydrous forsterite samples display an anharmonic behavior significantly stronger than that observed for other OH bands in the same frequency range (e.g. band 7a, Fig. 1a; the same band as the band at 3612 cm^{-1} of Yang & Keppler (2011)). Importantly, both bands are mostly polarized along Y ([010] axis) and their anharmonic behavior is quite similar. It consists in a significant frequency lowering (Fig. 1b) and band broadening (Fig. 1c) when the temperature increases from 79 to 473 K. This anharmonic behaviour was evaluated by Balan *et al*. (2014) using the Persson & Ryberg model of vibrational phase relaxation (Persson & Ryberg, 1985 a,b). In this model, the high-frequency localized vibrational mode (LVM) of a molecular group is anharmonically coupled to a single

so-called "exchange mode" at low frequency. The exchange mode is itself weakly coupled via a friction parameter η to the phonon bath of the host crystal. The following relations describe the temperature-dependence of the frequency shift, $\Delta\Omega = \Omega - \Omega_0$, and contribution to the width, $\Delta\Gamma = \Gamma - \Gamma_0$, of the high-frequency LVM band (here the OH-stretching band):

$$\Delta\Omega = \delta\omega/(\exp(h\omega_{ex}/2\pi kT)-1) \quad (1)$$

and

$$\Delta\Gamma = 2\,\delta\omega\,(\delta\omega/\eta)\,\exp(h\omega_{ex}/2\pi\,kT)\,/(\exp(h\omega_{ex}/2\pi kT)-1)^2 \quad (2)$$

where h is the Planck constant, k the Boltzmann constant and T the temperature. The parameters ω_{ex} is the harmonic angular frequency of the exchange mode and $\delta\omega$ describes the coupling between the high-frequency LVM and the exchange mode. A fit of the experimental Ω values as a function of temperature using Eq. 1 leads to a ω_{ex} frequency below 300 cm^{-1} and a $\delta\omega$ parameter of -32 and -52 cm^{-1} for the bands 3a and 8a (Balan *et al*., 2014). These values are entailed by a significant uncertainty related to the limited temperature range that can be experimentally explored and the significant overlap between experimental bands. A slightly different approach can be used to treat the experimental data, taking into account both the measured frequency and width. The contribution to the shift and width predicted by Eq. 1 and 2, respectively, becomes temperature independent and negligible at low temperature ($2\pi kT << h\omega_{ex}$). A residual temperature-independent contribution to the measured width arises from the spectrometer resolution (1 cm^{-1}, Ingrin *et al*., 2013) and inhomogeneous broadening. Assuming that the lowest measurement temperature is low enough to correspond to the saturation domain (Fig. 1b), the values of Ω_0 and the temperature-independent contribution to

225 the width (Γ_0) were assumed to be equal to those measured at 79K for the bands 3a and 8a
226 (Table 1). For the other bands, their width at 79 K is very close to the spectrometer resolution
227 and Γ_0 was set to 1 cm^{-1}. Following Dumas *et al*. (1990), the Persson & Ryberg model implies
228 that the logarithm of the quantity $\Delta\Gamma/(\Delta\Omega)^2$ is linearly related to the inverse of temperature:
229
230 $$\Delta\Gamma/(\Delta\Omega)^2=(2/\eta)\exp(h\omega_{ex}/2\pi kT) \quad (3)$$
231
232 Accordingly, a linear fit of related experimental data should lead to the values of ω_{ex}
233 and η. 0verall, the two anharmonic bands display a behavior consistent with this model (Fig
234 1d). In contrast, the other bands (4a, 5a and 7a) display a systematic departure from linearity.
235 The linear extrapolation to infinite temperature leads to η values of 137 and 438 cm^{-1} for the
236 bands 3a and 8a, respectively (Table 1). The ω_{ex} values extracted from the slope of the linear
237 fits are 387 and 470 cm^{-1}, respectively. These values of exchange frequencies are significantly
238 higher than those previously proposed in Balan *et al*. (2014) (242 and 270 cm^{-1}, respectively).
239 New fits of experimental OH stretching frequencies (Fig. 1b) were then performed by
240 constraining the ω_{ex} and Ω_0 parameters to the above values, leading to coupling parameters
241 ($\delta\omega$ = -68 and -142 cm^{-1} for band 3a and 8a, respectively) about three times stronger than
242 those obtained by Balan *et al*. (2014). At this stage, the broadening predicted by Eq. 2 is fully
243 determined by the coupling parameters $\delta\omega$, exchange mode frequencies ω_{ex}, friction parameter
244 η and Γ_0 values (Table 1). Comparing with experimental data (Fig. 1c), the new sets of
245 internaly consistent experimental parameters can account for the significant increase in the
246 width of bands 3a and 8a with temperature, even though the agreement between model and
247 experiment is not perfect. The adequation between model and experimental data is affected by
248 the difficulty to extract accurate parameters on overlapping bands as well as by the
249 simplifying assumptions of the model. Note that η is still significantly larger than $|\delta\omega|$, which

250 is roughly consistent with the weak coupling assumption of the Persson & Ryberg model. In
251 contrast, the significantly different behavior of the weakly anharmonic bands (4a, 5a, and 7a)
252 suggests that their temperature-dependance would be poorly described by such phase
253 relaxation mechanism involving a single exchange mode.
254
255 3.2 **Theoretical Raman spectrum and structural interpretation of OH-stretching bands**
256 **in forsterite**
257
258 By investigating the temperature dependence of the infrared absorption bands in the
259 spectrum of boron-bearing synthetic forsterite and natural olivine samples (containing up to
260 230 ppm and 72 wt. ppm of B, respectively), Ingrin *et al*. (2014) brought strong evidences
261 relating the band 8a (at 3598 cm^{-1} in room temperature spectra) to a hydroxyl group
262 associated to a trigonal boron group at the tetrahedral site of olivine. In the corresponding
263 atomic-scale theoretical model (B_H_1; Ingrin *et al*. 2014), the BO_3 group occupies the face
264 of the tetrahedron delimited by the O1 and the two symmetric O3 oxygen atoms (Fig. 2). The
265 H atom is bonded to the opposite O2 vertex and points away from the tetrahedron. Its
266 symmetric environment precludes a H-bond sharing with nearby oxygen atoms. This
267 environment displays a strong similarity with that of the O2 atom in the most stable
268 configuration of a four-fold protonated Si vacancy (referred to as Si_3; Balan *et al*., 2011). In
269 the Si_3 configuration, three OH groups are oriented along the edges of the tetrahedral sites,
270 sharing weak H-bonds with nearby OH groups, whereas the O2-H group points away from the
271 tetrahedron and is not H-bonded (Fig. 2). A comparison between the theoretical Si_3 defect
272 (Balan *et al*., 2011) and experimental (e.g., Lemaire *et al*., 2004; Mosenfelder *et al*., 2006;
273 Smyth *et al*., 2006; Kovács *et al*., 2010) infrared spectra indicates that the experimental bands
274 7a, 5a and 4a, characterized by a weakly anharmonic behaviour and room temperature

wavenumbers of 3613, 3579 and 3567 cm^{-1}, are dominantly related to the O1-H stretching and to two modes involving the coupled stretching motion of the O3-H groups, respectively. The Raman spectrum of hydrous forsterite (Hushur *et al*., 2009; Bolfan-Casanova *et al*., 2014) displays three bands at positions coinciding with that of bands 7a, 5a and 3a of the infrared spectrum (Fig. 3). Strong differences are observed in the relative intensities with a marked decrease of the intensity of band 7a in favour of band 5a. The band 4a is not observed in the Raman spectrum suggesting that its intensity is also very weak. The theoretical Raman spectrum (Fig. 3) correctly reproduces these relative intensity changes, thus supporting the theoretical interpretation given for these three bands. Despite a dominant contribution of the O1-H group, the low intensity of band 7a (calculated at 3592 cm^{-1}) is explained by the coupled stretching motion of O2-H and O3-H groups in opposition of phase with the stretching of the O1-H group. When the O1-H bond elongates the three other OH bonds shorten (Fig. 4). In this case, the polarizability change associated to the vibration mode is minimal. This weakens the Raman intensity of this band, which becomes dominated by a residual (XY) cross-polarization term (Fig. 3). In contrast, the displacement of H atoms located on the O3 oxygens increases the polarization associated to the mode, enhancing its infrared absorption. The intensity of the weak band 4a (calculated at 3520 cm^{-1}), which is polarized along the Z direction, is also related to terms of the Raman tensors involving a cross-polarization because it corresponds to an anti-symmetric stretching motion of O3-H groups with respect to the (XY) symmetry plane (Fig. 4). In contrast, the band 5a (calculated at 3540 cm^{-1}), which dominantly corresponds to a symmetric motion of O3-H groups with a lesser contribution of the O1-H group (Fig. 4), displays the strongest Raman intensity, with a dominant polarization along X. It also displays a significant infrared activity (Balan *et al*., 2011). However, neither the Raman spectra nor the low temperature FTIR spectra (Ingrin *et al*., 2013, 2014) reveal the presence of a weakly anharmonic band matching that theoretically

predicted for the O2-H group. Meanwhile, the band 3a appears as being systematically associated with the other bands of the Si_3 defect and is also observed at 3548.4 and 3550 cm^{-1} in the Raman spectra of forsterite reported by Huschur *et al*. (2009) and Bolfan-Casanova *et al*. (2014), respectively. Considering this convergent set of observations and the similar polarization and anharmonic properties of bands 3a and 8a, it becomes self-evident that the band 3a corresponds to the O2-H group in the Si_3 configuration of protonated silicon vacancies ($(4H)^{x}_{Si}$). Accordingly, the bands 3a, 4a, 5a and 7a (Ingrin *et al*., 2013) are all related to the vibration modes reported for this configuration in Balan *et al*. (2011). In this case, the band 3a at 3566 cm^{-1} (at 79 K, Fig. 1a) is observed at a frequency relatively lower than that expected from theory (c.a. 3600 cm^{-1}), a feature that could be linked to the stronger mode anharmonicity. Finally, the weak band at 3480 cm^{-1} in the experimental Raman spectrum is most likely related to a slightly less stable configuration of the $(4H)^{x}_{Si}$ defect (Balan *et al*., 2011). This structural interpretation of the hydrous forsterite spectrum is consistent with the prevalence of electroneutrality at atomic scale in defective ionic or iono-covalent crystals (Kröger & Vink, 1956; Nakamura & Schmalzried, 1983; Crépisson *et al*., 2014b).

3.3 Theoretical analysis of OH group anharmonicity

In this part, the contrasted anharmonic behavior exhibited by the O2-H groups in the B_H_1 and Si_3 defects compared to the other OH groups in the Si_3 defect is examined on a theoretical basis. The harmonic vibrational modes of both defects were first determined from the usual approach based on a diagonalization of the zone-center dynamical matrix (Table 3), leading to stretching frequencies consistent with the previous investigations (Balan *et al*., 2011; Ingrin *et al*., 2014). Then, the anharmonic coupling between (harmonic) vibrational

325 modes can be investigated by considering derivatives of the total energy with respect to
326 atomic displacements with orders higher than quadratic. For example, assuming an
327 anharmonic interaction potential between the modes Q_i of the form $V_{1122}=C_{1122}Q_{LVM}^2Q_{ex}^2$, the
328 parameter $\delta\omega$ is given by the following expression:
329
330 $$\delta\omega = \frac{h\, C_{1122}}{2\pi\, \tilde{m}_{LVM}\tilde{m}_{ex}\omega_{LVM}\omega_{ex}} \qquad (4)$$
331
332 where ω_{LVM} is the harmonic angular frequency of the LVM and $\tilde{m}_{LVM}$ and $\tilde{m}_{ex}$ are the effective
333 masses of the LVM and exchange mode (note that the $\delta\omega$ values in Balan *et al*. (2014) were
334 underestimated due to a wrong prefactor in the expression of C_{1122}).
335 In order to identify the exchange mode and to explain the strikingly different
336 anharmonic behaviour of the specific OH-stretching bands, we remind that the analysis of
337 measurements suggests that the specific behavior of proton at the O2 site is related to the
338 occurrence of an exchange mode at a frequency in the range 400 - 500 cm^{-1}. The analysis of
339 the vibrational properties of the cell simulated within DFT reveals that the displacement of the
340 H atoms transverse to the stretching direction is indeed associated to vibrations in that
341 frequency range. Unfortunately, the diagonalisation of the dynamical matrix of the full system
342 is not a viable approach to determine the properties of this mode since the transverse H
343 displacement turns out to be coupled to several distinct vibrational normal modes.
344 A more transparent understanding of the physics is obtained by analyzing the local
345 environment of OH groups. Focusing on O2-H and O1-H groups, which are both located on a
346 symmetry plane of the forsterite structure, the potential energy landscape related to
347 displacements of hydrogen atoms around their equilibrium position was built by calculating
348 the total energy of the system on a regular 2D grid of atomic positions (Fig. 5). The

coordinates of the displacements were defined in a local orthonormal reference frame. The longitudinal displacements δx are parallel to the OH bond and the transverse displacement δz are defined in the perpendicular plane, along the crystallographic *c*-axis of the forsterite structure. For δx ranging between -0.4 and +0.4 a_0 ($a_0 = 0.529177\ 10^{-10}$ m) and δz between -1.2 and +1.2 a_0, the surface corresponding to the B_H_1 model displays a complex shape. The short range O-H repulsion dominates for a longitudinal shortening of the bond whereas the potential is relatively flat in the transverse direction. A very similar potential shape was observed for the O2-H and O1-H groups of the Si_3 defect. Although the differences between the potential energy surfaces are not immediately apparent, a 2D polynomial fit of the surfaces performed on a more restricted displacement range (-0.4 and +0.4 atomic units for both coordinates) revealed significant variations in the quadratic transverse coefficient $(\delta z)^2$ (Table 3), which determines the exchange mode frequency. It is very remarkable, that the anharmonic coupling terms, such as the $(\delta x)^2(\delta z)^2$ one, are very similar for the three OH groups. This finding indicates that the differences of the anharmonic behavior of the three OH groups are not related to a difference of the coupling between the LVMs and the respective exchange modes but only to a difference of the exchange-mode frequencies. Why this change of the frequency of the soft transverse modes should have such a dramatic effect on the anharmonic behavior of the stretching modes cannot be understood solely within the Person & Ryberg model but is related to the specificities of the system under consideration.

The difference in the quadratic transverse coefficient is more apparent when considering 1D sections of the potential energy surface performed at coordinates δz=0 (longitudinal section) or δx=0 (transverse section) (Fig. 6). For the longitudinal section, the potential is almost identical for the three OH groups. It corresponds to a usual OH stretching potential, with significant cubic and quartic contributions (*e.g.*, Szalay *et al.*, 2002). It is also very close to the potential previously determined at the DFT level for inner-OH groups in

374 phyllosilicates (Balan *et al*., 2007). The weak H-bonding of the O1-H group only has a minor
375 effect on the potential shape, which is consistent with the high-values of the corresponding
376 harmonic stretching frequencies (Table 3). In contrast, the transverse sections reveal a more
377 significant difference in the potential shapes. The O2-H group in the B_H_1 and Si_3 defects
378 displays a very similar potential shape. It is characterized by a comparatively smaller value of
379 the quadratic term $(\delta z)^2$, which amounts to about one half of that determined for the O1-H
380 group. In contrast, the higher quadratic coefficient of the O1-H group reflects the highly
381 directional character of H-bonding (e.g. Wood *et al*., 2009). The harmonic frequencies
382 obtained by only considering the displacement of the H atom in this 1D potential are close to
383 450 cm^{-1} for the O2-H groups and 630 cm^{-1} for the O1-H group (Table 3). The same
384 frequencies within numerical errors are obtained by diagonalizing a partial dynamical matrix
385 restricted to the displacement of the H-atom only. The mean square displacements computed
386 for the corresponding modes (Table 2) however show that the H atoms move significantly
387 away from their equilibrium position, indicating that the harmonic model will only provide an
388 indicative picture of the proton dynamics.
389 Additional insight in the system dynamics can be achieved by extending the partial
390 dynamical matrix to the displacements of the O and H atoms belonging to the OH group. In
391 this case, the vibrational modes can be categorized as one stretching, two hindered rotation
392 and three hindered translations. The approach can also be easily extended to the O3-H groups,
393 which are located in an environment less symmetric than that of the O2-H and O1-H groups.
394 The stretching frequencies are very close to those obtained by diagonalizing the full
395 dynamical matrix, as previously observed (Balan *et al*., 2011). The hindered translation
396 modes are grouped between 270 and 470 cm^{-1}. The hindered rotation modes are observed
397 above 630 cm^{-1} for the O1-H and O3-H groups whereas one of these modes has its frequency
398 significantly lowered for the O2-H groups and is observed close to 500 cm^{-1} (Table 3),

399 consistent with the range expected for the exchange mode. It is thus suggested that a shift
400 from > 630 cm^{-1} to 500 cm^{-1} of this hindered rotation mode dramatically affects the
401 anharmonic properties of the OH groups. The other hindered rotation mode corresponding to
402 the orthogonal transverse displacement of the hydrogen is observed at 868, 881, 814 and 925
403 cm^{-1} for the O2-H (B_H_1 and Si_3 models), O1-H and O3-H groups, respectively. These
404 frequencies do not appear as related to the differences in the anharmonic character of OH
405 groups.
406 Although unexpected, the strong effect of the lowering of one of the hindered rotation
407 modes can be understood by considering the peculiar shape of the vibrational density of states
408 of forsterite. This density of states has been reported from experimental measurements (*e.g.*,
409 Rao *et al.*, 1988) and theoretical modeling (*e.g.*, Li *et al.*, 2007). It displays two regions which
410 are well separated by a gap observed between 620 and 820 cm^{-1}. The forsterite structure does
411 not display vibrational modes occurring between these two frequencies. The higher frequency
412 region is related to the dispersion of the internal Si-O stretching modes whereas the lower
413 region involves the dispersion of both internal SiO_4 bending modes and external modes. As a
414 consequence, the lowering of one of the hindered rotation frequency from 630 cm^{-1} to 500 cm^{-1}
415 is expected to introduce a more efficient coupling between this mode and the forsterite
416 phonon bath (Fig. 7). The peculiar anharmonic behavior of the O2-H groups is thus ascribed
417 to the coupling between the stretching LVM with a transverse hindered rotation mode that
418 efficiently relaxes to the phonon bath of the host. In this case, the relatively higher value of
419 the friction parameter η sustains a description of the anharmonic behavior in the weak
420 coupling limit corresponding to the Persson & Ryberg model. In contrast, the hindered
421 rotation modes of the O1-H and O3-H display similar coupling coefficients with the
422 stretching LVM but are much less efficiently coupled to the phonon bath. In this case, the

423 phase relaxation process of the OH stretching mode could involve its direct coupling to the
424 host phonon bath, a much less efficient process (Budde *et al*., 2001).
425

426 4. Crystal-chemical and mineralogical implications

427

428 The present results improve our understanding of the proton crystal-chemistry in
429 anhydrous minerals and solid materials and might provide a firmer basis to interpret
430 experimental petrology results and their extrapolation to inner-Earth processes.
431 Concerning the first aspect, they reveal an unusual relation between H-bonding and
432 anharmonicity. Isolated and weakly H-bonded OH groups are indeed expected to display a
433 weaker anharmonic character than more strongly H-bonded groups (Libowitzky & Beran,
434 2006). It is well established that stronger H-bonding decreases the stretching potential
435 curvature, decreasing the related stretching frequency, and increases its departure from a
436 parabolic function (Nakamoto et al., 1995, Libowitzky, 1999; Szalay et al., 2002, Balan et al.,
437 2007). A stronger H-bonding is also expected to decrease the lifetime of excited stretching
438 vibrational states, inducing a homogeneous broadening of the band. This relation can be
439 roughly described as follows. Infrared absorption corresponds to a coherent excitation of an
440 ensemble of oscillators. Accordingly, the decay of the excited state can occur either through
441 energy transfer from individual excited states to other vibrational states of the crystal
442 (population relaxation process) or through thermal fluctuations inducing a loss in the phase
443 coherence of the excited state (vibrational phase relaxation) (Bonn et al., 1996; Budde et al.,
444 2001; Martin et al. 2006). For high-energy OH stretching modes, population relaxation is not
445 an efficient process because energy conservation requires a coupling with a large number of
446 the host vibrational states. The observed broadening of OH stretching bands is thus dominated
447 by dephasing processes, which can also occur, at least, through two different mechanisms.

448 Increasing the H-bond strength can directly strengthen the stochastic modulation of the
449 stretching vibration of the H-bonded OH group or can enhance the population relaxation of a
450 low frequency exchange mode anharmonically coupled to the OH stretching mode. The two
451 mechanisms have been shown to occur, depending on the specificities of OH group
452 environment (Bonn et al., 1996). According to the present results, the thermal-behaviour of
453 high-frequency anharmonic OH bands in the infrared spectrum of hydrous forsterite can be
454 accounted for by the second mechanism. In this case, the reverse relation observed between
455 H-bonding and band broadening results both from the softening of the transverse motion of H
456 atoms not involved in a directional H-bond and from the specific shape of the forsterite
457 vibrational density of states.

458 As H-bonding usually tends to increase the Born effective charge of the H atom, it
459 leads to a related increase in the mode polarization and infrared absorption coefficient that can
460 be correlated to the lowering of OH stretching frequency (Paterson, 1982; Libowitzky &
461 Rossman, 1997; Balan et al., 2008). This dependance is commonly used to quantify OH
462 defects in nominally anhydrous minerals using infrared spectroscopy (Bell et al., 2003; Koch-
463 Müller & Rhede, 2010; Kovács et al., 2010). In the present case, the longitudinal dynamics of
464 H atoms is similar for the different OH groups investigated and the OH quantification
465 procedure should not be affected. Indeed, it is expected that the absorption coefficient of the
466 anharmonic infrared absorption band will be similar to that inferred for the other bands
467 occurring in the similar frequency range. The peculiar anharmonic behavior observed as a
468 function of temperature is not expected to dramatically affect their absorption coefficient.
469 Moreover, the anharmonic bands 3a and 8a do not reveal any peculiar temperature variation
470 of their integrated area (Ingrin et al., 2013).

471 The present structural interpretation of the infrared and Raman spectrum of OH
472 stretching bands in forsterite relates the bands 3a, 4a, 5a and 7a (Ingrin et al., 2013) to the

vibration modes of the same $(4H)_{Si}^{x}$ defect (the previous attempt to relate the band 3a to the presence of interstitial OH groups (Balan et al., 2014) should not be considered any more as the most valid hypothesis). As a consequence, the incorporation of hydrogen at tetrahedral sites appears as the dominant incorporation mechanisms and this mechanism should be included in the thermodynamic models of water solubility in forsterite. The observation of similar defects in iron-bearing systems suggests that this conclusion can be most likely extended to olivine (Blanchard et al., 2016). The implications for the solubility laws of water in forsterite and olivine are discussed in Ingrin et al. (2013) and more recently in Blanchard et al. (2016). Note that given the rarity of natural olivine samples with significant boron concentration, the $(B,H)_{Si}^{x}$ defect is not expected to play any major control in the hydrogen speciation in the Earth upper mantle.

Beside the identification of the defects, the determination of the corresponding vibrational modes makes it possible to discuss in more details some of the changes in the infrared spectrum of olivine observed as a function of temperature (Yang & Keppler, 2011). Indeed, the disappearance above 400 °C of the band observed at 3612 cm^{-1} at room temperature (band 7a) has been interpreted as revealing a temperature dependent equilibrium between two different proton sites. The present results show that this band is not related to a single OH group but involves the coupled stretching of the four OH groups of a $(4H)_{Si}^{x}$ defect and, most important, that its infrared and Raman intensities are highly dependent on the coupling scheme. Thus, the behaviour reported by Yang & Keppler (2011) could be simply due to a change in the H-bonding geometry and does not necessarily involve a proton migration between different sites at high-temperature. The nature of the OH defects in quenched samples could correctly reflect the high-temperature mechanism of water dissolution in olivine, as commonly assumed before Yang & Keppler (2011). A high-temperature configurational equilibrium can be expected from the previous identification of

several stable configuration of the $(4H)_{Si}^{x}$ defect with small energy differences (Umemoto et al., 2011; Balan et al., 2011). As the multiple configurations of the defect contribute to the system entropy, they could stabilize $(4H)_{Si}^{x}$ defects at high temperature. Further studies would be required to better understand the contrasted relative stability of tetrahedral defects observed between olivine and orthopyroxene (Prechtel & Stalder, 2011). As a matter of fact, the OH bands at high frequencies related to the $(4H)_{Si}^{x}$ defects, including the broad band at 3550 cm^{-1} are systematically dominant for olivine or forsterite synthesized in presence of orthopyroxene (see for example, Otsuka & Karato, 2011, Withers et al., 2011, Férot & Bolfan-Casanova, 2012).

Acknowledgments: This work was performed using HPC resources from GENCI-IDRIS (Grant 2016-i2009041519). This work was supported by CNRS through a grant from the INSU 2016-PNP program. We thank I. Kovács and one anonymous reviewer for their constructive comments.

References

Bai, Q. &Kohlstedt, D.L. (1993): Effects of chemical environment on the solubility and incorporation mechanism for hydrogen in olivine. *Phys. Chem. Minerals,* **19**, 460-471.

Balan, E., Lazzeri, M., Delattre, S., Meheut, M., Refson, K., Winkler, B. (2007): Anharmonicity of inner-OH stretching modes in hydrous phyllosilicates: Assessment from first-principles frozen-phonon calculations. *Phys. Chem. Minerals,* **34**, 621-625.

521 Balan, E., Refson, K., Blanchard, M., Delattre, S., Lazzeri, M., Ingrin, J., Mauri, F., Wright,
522 K., Winkler, B. (2008): Theoretical infrared absorption coefficient of OH groups in
523 minerals. *Am*. *Mineral*., **93**, 950-953.
524 Balan, E., Ingrin, J., Delattre, S., Kovacs, I., Blanchard, M. (2011): Theoretical infrared
525 spectrum of OH-defects in forsterite. *Eur*. *J*. *Mineral*., **23**, 285-292.
526 Balan, E., Blanchard, M., Lazzeri M., Ingrin, J. (2014): Contribution of interstitial OH groups
527 to the incorporation of water in forsterite. *Phys*. *Chem*. *Minerals*, **41**, 105-114.
528 Baroni, S., de Gironcoli, S., Dal Corso, A., Giannozzi, P. (2001): Phonons and related crystal
529 properties from density-functional perturbation theory. *Rev*. *Modern Phys*., **73**, 515-
530 561.
531 Bell, D.R. & Rossman, G.R (1992): Water in earth's mantle: the role of nominally anhydrous
532 minerals. *Science*, **255**, 1391–1397.
533 Bell, D.R., Rossman, G.R., Maldener, J., Endisch, D., Rauch, F. (2003): Hydroxide in olivine:
534 A quantitative determination of the absolute amount and calibration of the IR spectrum.
535 *J*. *Geophys*. *Res*., **108**, B2, 2105-2113.
536 Beran, A. & Zemman, J. (1969): Über OH-gruppen in Olivin. *Öster*. *Akad*. *Wiss*., **3**, 73-74.
537 Beran, A. & Putnis, A. (1983): A model of the OH position in olivine, derived from infrared-
538 spectroscopy investigations. *Phys*. *Chem*. *Minerals*, **9**, 57-60.
539 Beran, A. & Libowitzky E. (2006): Water in Natural Mantle Minerals II: Olivine, Garnet and
540 Accessory Minerals. *Rev*. *Mineral*. *Geochem*., **62**, 169-191.
541 Berry, A.J., Hermann, J., O'Neill, H.S.C., Foran, G.J. (2005): Fingerprinting the water site in
542 mantle olivine. *Geology*, **33**, 869-872.
543 Berry, A.J., O'Neill, H.S.C., Hermann, J., Scott, D.R. (2007): The infrared signature of water
544 associated with trivalent cations in olivine. *Earth Planet*. *Sci*. *Lett*., **261**, 134-142.

545 Blanchard, M., Ingrin, J., Kovács I., Withers A.C. (2016): Effect of iron and trivalent cations
546 on OH-defects in olivine. *Am*. *Mineral*., (paper with Editor for final decision)
547 Bolfan-Casanova, N. (2005): Water in the Earth's mantle. *Mineral*. *Mag*., **69**, 229-257
548 Bolfan-Casanova, N., Montagnac, G., Reynard, B. (2014): Measurement of water contents in
549 olivine using Raman spectroscopy. *Am*. *Mineral*., **99**, 149-56.
550 Bonn, M., Brugmans, M.J., Kleyn, A.W., van Santen, R.A., Bakker, H.J. (1996): Vibrational
551 dephasing mechanisms in hydrogen-bonded systems. *Phys*. *Rev*. *Lett*., **76**, 2440-2443.
552 Budde, M., Parks Cheney, C., Lüpke, G., Tolk, N.H., Feldman, L.C. (2001): Vibrational
553 dynamics of bond-center hydrogen in crystalline silicon. *Phys*. *Rev*. *B*, **63**, 195203.
554 Chopra, P.N. & Paterson, M.S. (1984): The role of water in the deformation of dunite. *J*.
555 *Geophys*. *Res*., **89**, 7861-7876.
556 Crépisson, C., Blanchard, M., Bureau, H., Sanloup, C., Withers, A.C., Khodja, H., Surblé, S.,
557 Béneut, K., Leroy, C., Giura, P., Balan, E. (2014a): Clumped fluoride-hydroxyl
558 defects in forsterite: Implications for the upper-mantle. *Earth Planet*. *Sci*. *Lett*., **390**,
559 287-295.
560 Crépisson, C., Bureau, H., Blanchard, M., Ingrin, J., Balan, E. (2014b): Theoretical infrared
561 spectrum of partially protonated cationic vacancies in forsterite. *Eur*. *J*. *Mineral*., **26**,
562 203-210.
563 Damen, T.C., Porto, S.P.S., Tell, B. (1966): Raman effect in zinc oxide. *Phys Rev*, **142**, 570–
564 574.
565 Demouchy, S., Tommasi, A., Barou, F., Mainprice, D., Cordier, P. (2012): Deformation of
566 olivine in torsion under hydrous conditions. *Phys*. *Earth Planet*. *Int*., 202-203, 57-70.
567 Demouchy, S. & Bolfan-Casanova, N. (2016): Distribution and transport of hydrogen in the
568 lithospheric mantle: A review. *Lithos*, **240-243**, 402-425.

569 Dumas, P., Chabal, Y.J., Higashi, G.S. (1990): Coupling of an adsorbate vibration to a
570 substrate surface phonon: H on Si(111). *Phys*. *Rev*. *Lett*., **65**, 1124-1127.
571 Férot, A. & Bolfan-Casanova, N. (2012): Water storage capacity in olivine and pyroxene to
572 14 GPa: Implications for the water content of the Earth's upper mantle and nature of
573 seismic discontinuities. *Earth Planet*. *Sci*. *Lett*., **349-350**, 218-230.
574 Giannozzi, P., Baroni, S., Bonini, N., Calandra, M., Car, R., Cavazzoni, C., Ceresoli, D.,
575 Chiarotti, G.L., Cococcioni, M., Dabo, I., Dal Corso, A., de Gironcoli, S., Fabris, S.,
576 Fratesi, G., Gebauer, R., Gerstmann, U., Gougoussis, C., Kokalj, A., Lazzeri, M.,
577 Martin-Samos, L., Marzari, N., Mauri, F., Mazzarello, R., Paolini, S., Pasquarello, A.,
578 Paulatto, L., Sbraccia, C., Scandolo, S., Sclauzero, G., Seitsonen, A.P., Smogunov, A.,
579 Umari, P., Wentzcovitch, R.M. (2009): Quantum ESPRESSO: a modular and open-
580 source software project for quantum simulations of materials. *J*. *Phys*.*: Condens*.
581 *Matter*., **21**, 395502.
582 Gose, J., Schmädicke, E., Markowitz, M., Beran, A. (2009): OH point defects in olivine from
583 Pakistan. *Miner*. *Petrol*., **99,** 105-111.
584 Grant, K.J., Brooker, R.A., Kohn, S.C., Wood, B.J. (2007): The effect of oxygen fugacity on
585 hydroxyl concentrations and speciation in olivine: Implications for water solubility in
586 the upper mantle. *Earth Planet*. *Sci*. *Lett*., **261**, 219-229.
587 Hushur, A., Manghani, M.H., Smyth, J.R., Nestola, F., Frost, D.J. (2014): Crystal chemistry
588 of hydrous forsterite and its vibrational properties up to 41 GPa. *Am*. *Mineral*., **94**,
589 751-760.
590 Ingrin, J., Liu, J., Depecker, C., Kohn, S.C., Balan, E., Grant, K.J. (2013): Low-temperature
591 evolution of OH bands in synthetic forsterite, implication for the nature of H-defects
592 at high pressure. *Phys*. *Chem*. *Minerals*, **40**, 499-510.

593 Ingrin, J., Kovács, I., Deloule, E., Balan, E., Blanchard, M., Kohn, S.C., Hermann, J. (2014):
594 Identification of hydrogen defects linked to boron substitution in synthetic forsterite
595 and natural olivine. *Am*. *Mineral*., **99**, 2138-2141.
596 Koch-Müller, M., Matsyuk, S.S., Rhede, D., Wirth, R., Khisina, N. (2006): Hydroxyl in
597 mantle olivine xenocrysts from the Udachnaya kimberlite pipe. *Phys*. *Chem*. *Minerals*,
598 **33**, 276-287.
599 Koch-Müller, M. & Rhede, D. (2010): IR absorption coefficients for water in nominally
600 anhydrous high-pressure minerals. *Am*. *Mineral*., **95**, 770-775
601 Kohlstedt, D.J., Keppler, H., Rubie, D.C. (1996): Solubity of water in the α, β, and γ phases
602 of $(Mg,Fe)_2SiO_4$. *Contrib*. *Mineral*. *Petrol*., **123**, 345-357.
603 Kovács, I., O'Neill, H.St.C., Hermann, J., Hauri, E.H. (2010): Site-specific infrared OH
604 absorption coefficients for water substitution into olivine. *Am*. *Mineral*., **95**, 292-299.
605 Kröger, F.A. & Vink, H.J. (1956): Relation between the concentrations of imperfections in
606 crystallines solids. *Sol*. *State Phys*., Vol. 3, p. 307. Academy Press, New York.
607 Lazzeri, M., & Mauri, F. (2003): First principles calculation of vibrational Raman spectra in
608 large systems: signature of small rings in crystalline SiO_2. *Phys*. *Rev*. *Lett*., **90**,
609 036401.
610 Lemaire, C., Kohn, S.C., Brooker, R.A. (2004): The effect of silica activity on the
611 incorporation mechanism of water in synthetic forsterite: a polarised infrared
612 spectroscopic study. *Contrib*. *Mineral*. *Petrol*., **147**, 48-57.
613 Li, L, Wentzcovitch, R.M., Weidner, D.J., Da Silva, C.R.S. (2007): Vibrational and
614 thermodynamic properties of forsterite at mantle conditions. *J*. *Geophys*. *Res*., **112**,
615 B05206.
616 Libowitzky, E. & Beran, A. (1995): OH defects in forsterite. *Phys*. *Chem*. *Minerals*, **22**, 387-
617 392.

618 _ & _ (2006): The structure of hydrous species in nominally anhydrous minerals: Information
619 from polarized IR spectroscopy. *Rev*. *Mineral*. *Geochem*., **62**, 29-52.
620 Libowitzky, E. & Rossman, G.R. (1997): An IR absorption calibration for water in minerals.
621 *Am*. *Mineral*., **82**, 1111-1115.
622 Libowitzky, E. (1999): Correlation of OH stretching frequencies and O-H...O hydrogen bond
623 length in minerals. *Mh*. *Chem*., **130**, 1047-1059.
624 Mackwell, S.J., Kohlstedt, D.L., Paterson, M.S. (1985): The role of water in the deformation
625 of olivine single crystals. *J*. *Geophys*. *Res*., **90**, 11319-11333.
626 Martin, K.R., Blaney, P., Shi, G., Stavola, M., Fowler, W.B. (2006): Temperature dependence
627 of the vibrational spectrum of a Li-OH complex in ZnO: Infrared absorption
628 experiments and theory. *Phys Rev B*, **73**, 232509.
629 Matsyuk, S.S. & Langer, K. (2004): Hydroxyl in olivines from mantle xenoliths in
630 kimberlites of the Siberian platform. *Contrib*. *Mineral*. *Petrol*., **147**, 413-437.
631 Matveev, S., O'Neill H.St.C., Ballhaus, C., Taylor, W.R., Green, D.H. (2001): Effect of silica
632 activity on OH-IR spectra of olivine: implications for low-aSiO_2 mantle
633 metasomatism. *J*. *Petrol*., **42**, 721-729.
634 Matveev, S., Portnyagin, M., Ballhaus, C., Brooker, R.A., Geiger, C.A. (2005): FTIRS
635 spectrum of phenocryst olivine as an indicator of silica saturation in magmas. *J*.
636 *Petrol*., **46**, 605-614.
637 Matveev, S. & Stachel T. (2009): Evaluation of kimberlite diamond potential using FTIR
638 spectroscopy of xenocrystic olivine. *Lithos*, **112**, 36-40.
639 Mei, S. & Kohlstedt, D.L. (2000): Influence of water on plastic deformation of olivine
640 aggregates 2. Dislocation creep regime. *J*. *Geophys*. *Res*., **105**, 21471-21481.
641 Mosenfelder, J.L., Deligne, N.I., Asimow, P.D., Rossman, G.R. (2006): Hydrogen
642 incorporation in olivine from 2-12 GPa. *Am*. *Mineral*., **91**, 285-294.

643 Nakamoto, K., Margosches, M., Rundle, R.E. (1955): Stretching frequencies as a function of
644 distances in hydrogen bonds. *J*. *Am*. *Chem*. *Soc*., **77**, 831–857.
645 Nakamura, A. & Schmalzried, H. (1983): On the nonstoichiometry and point defects of
646 olivine. *Phys*. *Chem*. *Minerals*, **10**, 27-37.
647 Paterson, M.S. (1982): The determination of hydroxyl by infrared absorption in quartz,
648 silicate glasses and similar materials. *Bull*. *Minéral*., **105**, 20-29.
649 Perdew, J.P., Burke, K., Ernzerhof, M. (1996): Generalized Gradient Approximation Made
650 Simple. *Phys*. *Rev*. *Lett*., **77**, 3865–3868.
651 Persson, B.N.J. & Ryberg, R. (1985a): Vibrational phase relaxation at surfaces: CO on
652 Ni(111). *Phys*. *Rev*. *Lett*., **54**, 2119-2122.
653 _ & _ (1985b): Brownian motion and vibrational phase relaxation at surfaces: CO on Ni(111).
654 *Phys Rev B*, **32**, 3586-3596.
655 Prechtel, F. & Stalder, R. (2011): The potential use of OH-defects in enstatite as
656 geobarometer. *Contrib*. *Mineral*. *Petrol*., **162**, 615-623.
657 Rao, K., S.L. Chaplot, N. Choudury, S. Ghose, J.M. Hastings, L.M. Corliss (1988): Lattice
658 dynamics and inelastic neutron scattering from forsterite, Mg_2SiO_4: phonon dispersion
659 relation, density of states, and specific heat. *Phys*. *Chem*. *Minerals*, **16**, 83-97.
660 Smyth, J.R., Frost, D.J., Nestola, F., Holl, C.M., Bromiley, G. (2006): Olivine hydration in
661 the deep upper mantle: effects of temperature and silica activity. *Geophys*. *Res*. *Lett*.,
662 **33,** L15301.
663 Szalay, V., Kovács, L., Wöhlecke, M., Libowitzky, E. (2002): Stretching potential and
664 equilibrium length of the OH bonds in solids. *Chem*. *Phys*. *Lett*., **354**, 56-61.
665 Tasaka, M., Zimmeramn, M.E., Kohlstedt., D.L. (2015): Creep behavior of Fe-bearing olivine
666 under hydrous conditions. *J*. *Geophys*. *Res*., **120**, 6039-6057.

667 Umemoto, K., Wentzcovitch, R.M., Hirschmann, M.M., Kohlstedt, D.L., Withers, A.C.
668 (2011): A first-principles investigation of hydrous defects and IR frequencies in
669 forsterite: The case for Si vacancies. *Am*. *Mineral*., **96**, 1475-1479.
670 Walker, A.M., Demouchy, S., Wright, K. (2006): Computer modelling of the energies and
671 vibrational properties of hydroxyl groups in α- and β-Mg_2SiO_4. *Eur*. *J*. *Mineral*., **18**,
672 529-543.
673 Walker, A.M., Hermann, J., Berry, A.J., O'Neill, H.St.C. (2007): Three water sites in upper
674 mantle olivine and the role of titanium in the water weakening mechanism. *J*. *Geophy*.
675 *Res*., **112**, B05211.
676 Wilkins, R.W.T. & Sabine, W. (1973): Water content of some nominally anhydrous silicates.
677 *Am*. *Mineral*., **58**, 508-516.
678 Withers, A.C., Hirschmann, M.M., Tenner T.J. (2011): The effect of Fe on olivine H_2O
679 storage capacity: Consequences for H_2O in the martian mantle. *Am*. *Mineral*., **96**,
680 1039-1053.
681 Withers, A.C., Bureau, H., Raepsaet, C., Hirschmann, M.M. (2012): Calibration of infrared
682 spectroscopy by elastic recoil detection analysis of H in synthetic olivine. *Chem*.
683 *Geol*., **334**, 92–98.
684 Wood, P.A., Allen, F.H., Pidcock, E. (2009): Hydrogen-bond directionality at the donor H
685 atom—analysis of interaction energies and database statistics. *CrystEngComm*, **11**,
686 1563-1571.
687 Xue, X., Kanzaki, M., Turner, D., Loroch, D. (2016): Hydrogen incorporation mechanisms in
688 forsterite: ^{1}H NMR measurement and first- principles calculation. *Goldschmidt*
689 *Conference Abstracts* 3503.
690 Yang, X. & Keppler, H. (2011): In-situ infrared spectra of OH in olivine to 1100℃. *Am*.
691 *Mineral*., **96**, 451-454.

692

693

694
695

Figure captions:

Figure 1: (a) Experimental infrared spectrum of hydrous forsterite at low temperature (Ingrin *et al*. 2013). Individual contributions obtained from spectral decomposition have been shifted for clarity. The bands 3a and 8a represent 14% and 23% of the total absorbance, respectively. (b) Wavenumber of bands 3a, 7a and 8a as a function of temperature. The full lines correspond to constrained fits using Eq. 1 (see text). (c) Full-width at half maximum of bands 3a, 7a and 8a as a function of temperature. The lines correspond to the model behaviour determined from the fits of Fig. 1a and 1d. (d) $\ln(\Delta I/(\Delta\Omega)^2)$ as a function of T^{-1}. The point at 79K has not been included in the linear fit of band 3a and 8a. The behaviour of bands 4a, 5a and 7a is reported for comparison .

Figure 2: Models of protonated cationic vacancies in forsterite. The B_H_1 model corresponds to the most stable configuration of the clumped $(B, H)^{x}_{Si}$ defect reported by Ingrin *et al*. (2014). The Si_3 model corresponds to the most stable configuration of the $(4H)^{x}_{Si}$ defect reported by Balan *et al*. (2011). The O2-H environment is similar in both defects. The O3-H and O1-H in the Si_3 models share weak H-bonds with nearby OH groups. (note: X=[100]=γ, Y=[010]=α and Z=[001]=β)

Figure 3: Theoretical polarized Raman spectra of hydrous forsterite modeled using a lorentzian broadening of 3 cm^{-1}. Spectra are described using the Porto notation, $k_i(E_iE_s)k_s$, where the two symbols inside the parenthesis are the polarization of the incident and scattered light, while the ones outside are, from left to right, the propagation directions of the incident and scattered light, respectively (Damen *et al*., 1966). Band positions are specified in cm^{-1}.

721 The inset shows the room temperature experimental Raman spectrum of sample 691 from
722 Bolfan-Casanova *et al*. (2014). The correspondence with the bands 7a, 5a and 3a identified in
723 the infrared spectra is indicated. The band at 3480 cm^{-1} corresponds to a different
724 configuration of $(4H)^{x}_{Si}$ defect (Balan *et al*., 2011).
725
726 Figure 4: Scheme of hydrogen cartesian displacements for the stretching modes of the Si_3
727 model of $(4H)^{x}_{Si}$ defect. The displacement vectors have been obtained from the corresponding
728 eigenvectors of the dynamical matrix and the theoretical frequency is reported. Experimental
729 band labelling and room temperature frequency are reported in parenthesis.
730
731 Figure 5: Potential energy surface determined for longitudinal δx and transverse δz
732 displacements of the H atom in the B_H_1 model of $(B,H)^{x}_{Si}$ defect. Note the peculiar shape
733 of the potential. The spatial extension of atomic displacements is consistent with the ground
734 state delocalization of the H atom (Table 2).
735
736 Figure 6: Potential energy curves corresponding to sections of the potential energy surface
737 along the longitudinal and transverse directions for the O2-H and O1-H groups.
738
739 Figure 7: Theoretical frequencies of hindered translation (short vertical bars) and rotation
740 (long vertical bars) modes of OH groups obtained from partial dynamical matrix. The shaded
741 areas are covered by the phonon density of states of forsterite (Li *et al*., 2007). The peculiar
742 anharmonic properties of O2-H groups are ascribed to their significant interaction with the
743 vibrations of the crystal through hindered rotation modes.

744

745 Table 1: Spectroscopic and mode-coupling parameters obtained from experimental data

band	ω_0 (cm^{-1})	Γ_0 (cm^{-1})	ω_{ex} (cm^{-1})	$\delta\omega$ (cm^{-1})	η (cm^{-1})
3a	3566.2	4.8	387	-68	137
8a	3617.2	4.4	470	-142	438

746

747

Table 2: Coefficients of the polynomial fit of potential energy surfaces for longitudinal δx and transverse δz displacements. The corresponding polynomial function is $E(x,z) = a\,(\delta x)^2 + b\,(\delta x)^3 + c\,(\delta x)^4 + d\,(\delta z)^2 + e\,(\delta z)^2(\delta x) + f\,(\delta z)^2(\delta x)^2 + g\,(\delta z)^2(\delta x)^3 + h\,(\delta z)^2(\delta x)^4 + i\,(\delta z)^4 + j\,(\delta z)^4(\delta x) + k\,(\delta z)^4(\delta x)^2$, where the energy is in Rydberg and the displacements in atomic units (a_0). Note that terms related to odd powers of (δz) are zero because of the system symmetry.

coefficient	displacements	std. error	B_H_1	Si_3 (O2-H)	Si_3 (O1-H)
a	$(\delta x)^2$	+/- 0.001	0.471	0.459	0.459
b	$(\delta x)^3$	+/- 0.001	-0.581	-0.571	-0.587
c	$(\delta x)^4$	+/- 0.006	0.396	0.391	0.396
d	$(\delta z)^2$	+/- 0.001	0.008	0.008	0.016
e	$(\delta z)^2(\delta x)$	+/- 0.003	0.243	0.239	0.255
f	$(\delta z)^2(\delta x)^2$	+/- 0.02	-0.589	-0.578	-0.587
g	$(\delta z)^2(\delta x)^3$	+/- 0.01	0.658	0.644	0.658
h	$(\delta z)^2(\delta x)^4$	+/- 0.08	-0.603	-0.589	-0.605
i	$(\delta z)^4$	+/- 0.01	0.025	0.025	0.024
j	$(\delta z)^4(\delta x)$	+/- 0.02	-0.249	-0.244	-0.250
k	$(\delta z)^4(\delta x)^2$	+/- 0.08	0.449	0.438	0.449

Table 3: Harmonic theoretical properties of transverse (δx=0) and longitudinal (δz=0) OH vibrational modes

	model	quadratic coefficient (Ry/a_0^2)	frequency (H) (cm^{-1})	frequency (H DM) (cm^{-1})	frequency (OH DM) (cm^{-1})	frequency (full DM) (cm^{-1})	σ (a_0)
δx=0	B_H_1	0.008	472	450	510	-	0.25
	Si_3 (O2-H)	0.008	450	437	497	-	0.25
	Si_3 (O1-H)	0.016	645	631	638	-	0.21
δz=0	B_H_1	0.471	3513	3518	3618	3618	0.09
	Si_3 (O2-H)	0.459	3470	3474	3574	3573	0.09
	Si_3 (O1-H)	0.458	3467	3471	3578	3592	0.09
	Si_3 (O3-H)	-	-	3434	3536	3540, 3520	-

Notes: harmonic frequencies are obtained from the quadratic polynomial coefficient of potential energy and motion of H atom only (H); the partial dynamical matrix restricted to H atom (H DM); the partial dynamical matrix restricted to OH group (OH DM); and the full dynamical matrix (full DM). The minor differences with previous studies (Balan *et al*., 2011; Ingrin *et al*., 2014) are related to the more stringent convergence criteria imposed on the forces for the defect relaxation. Note that the full dynamical matrix does not enable a clear identification of transverse modes. The standard deviation of the modes $\sigma = \sqrt{\frac{h}{4\pi m \omega}}$ is obtained from the quadratic polynomial coefficient of potential energy and motion of H atom only. It reflects the ground-state delocalization of the H atom.

Figure 1

Click here to download Figure Fig1_rev.jpg

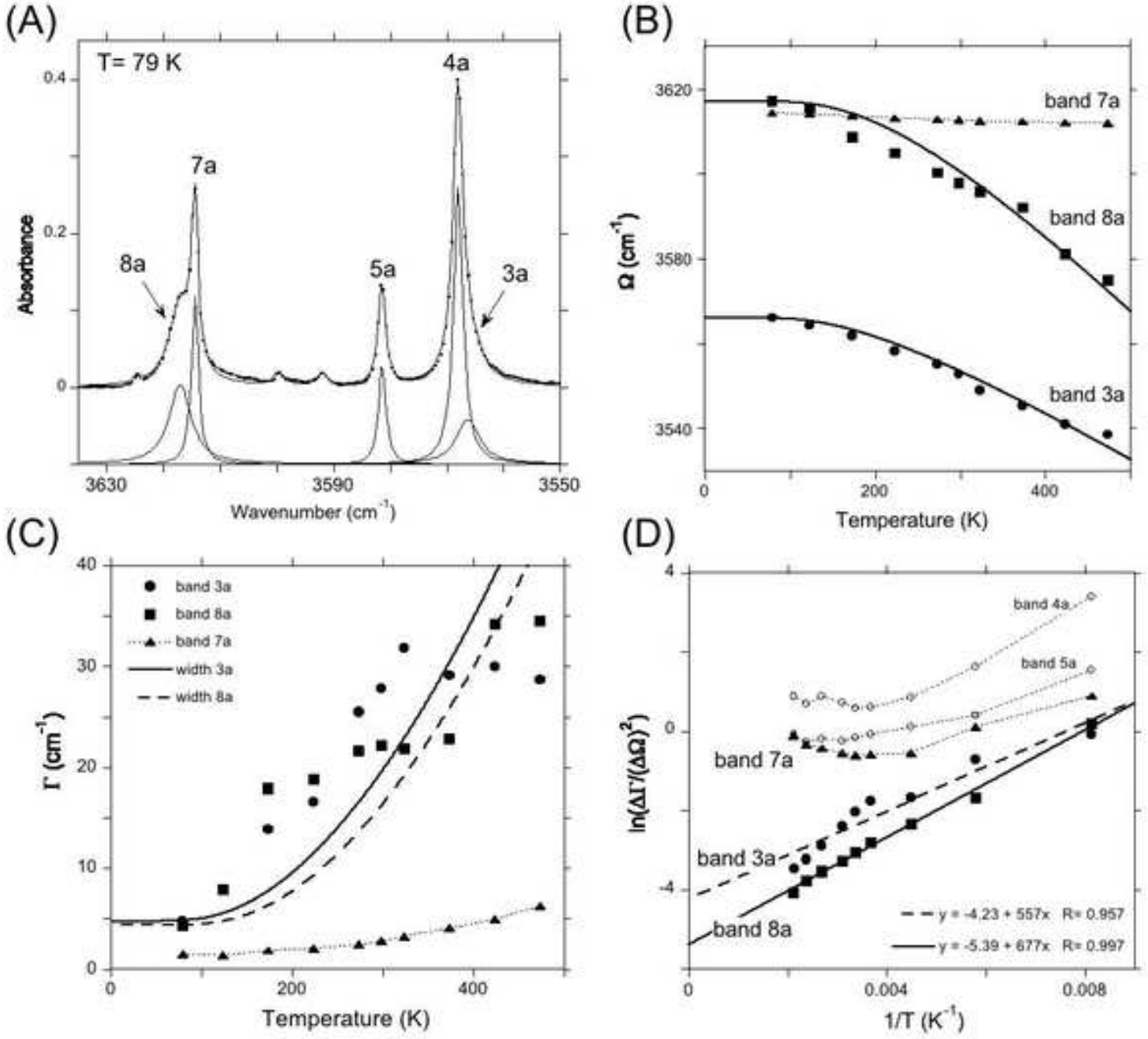

Figure 2

Click here to download Figure Fig2_rev.jpg

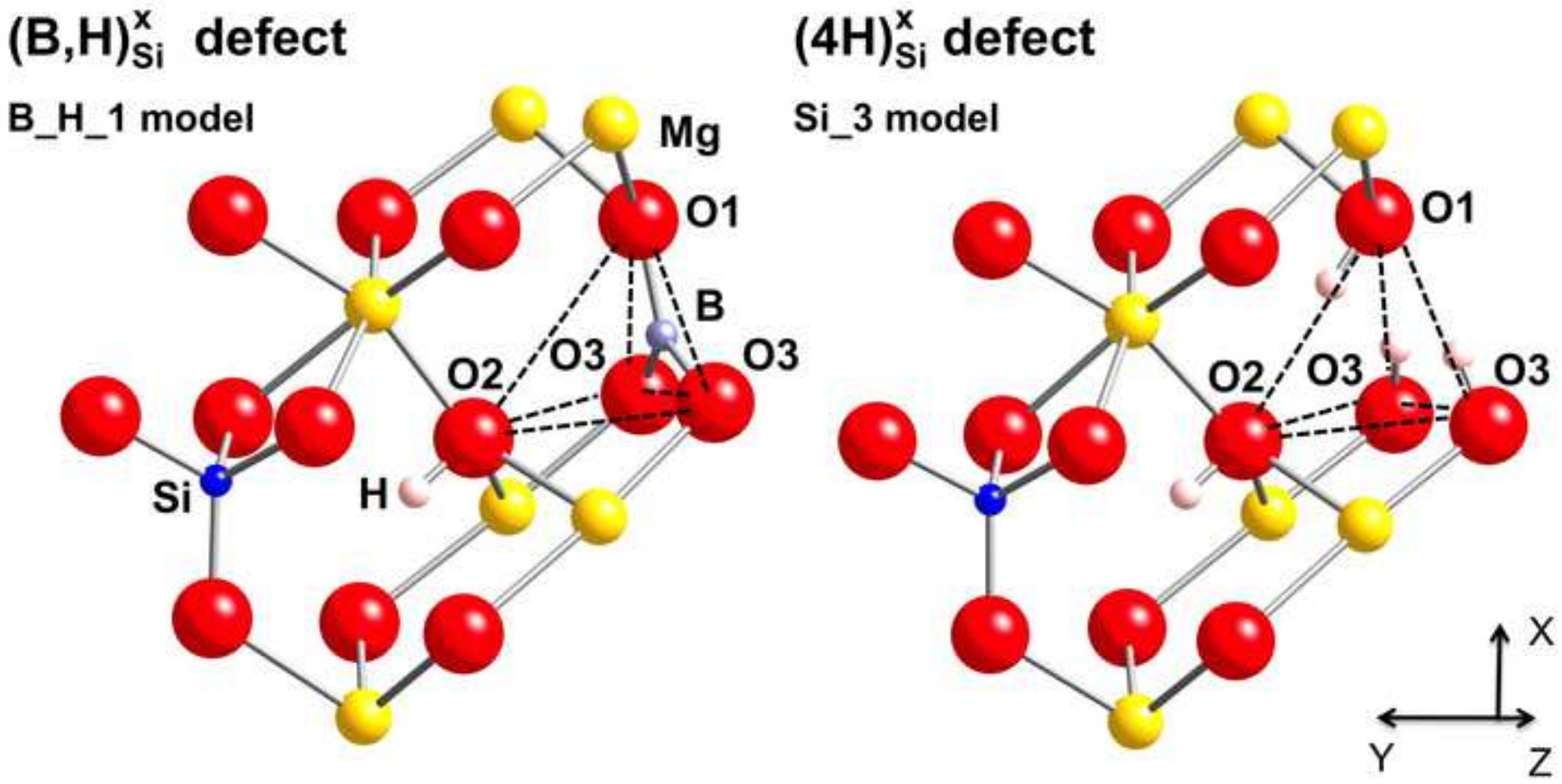

Figure 3

Click here to download Figure Fig3.jpg

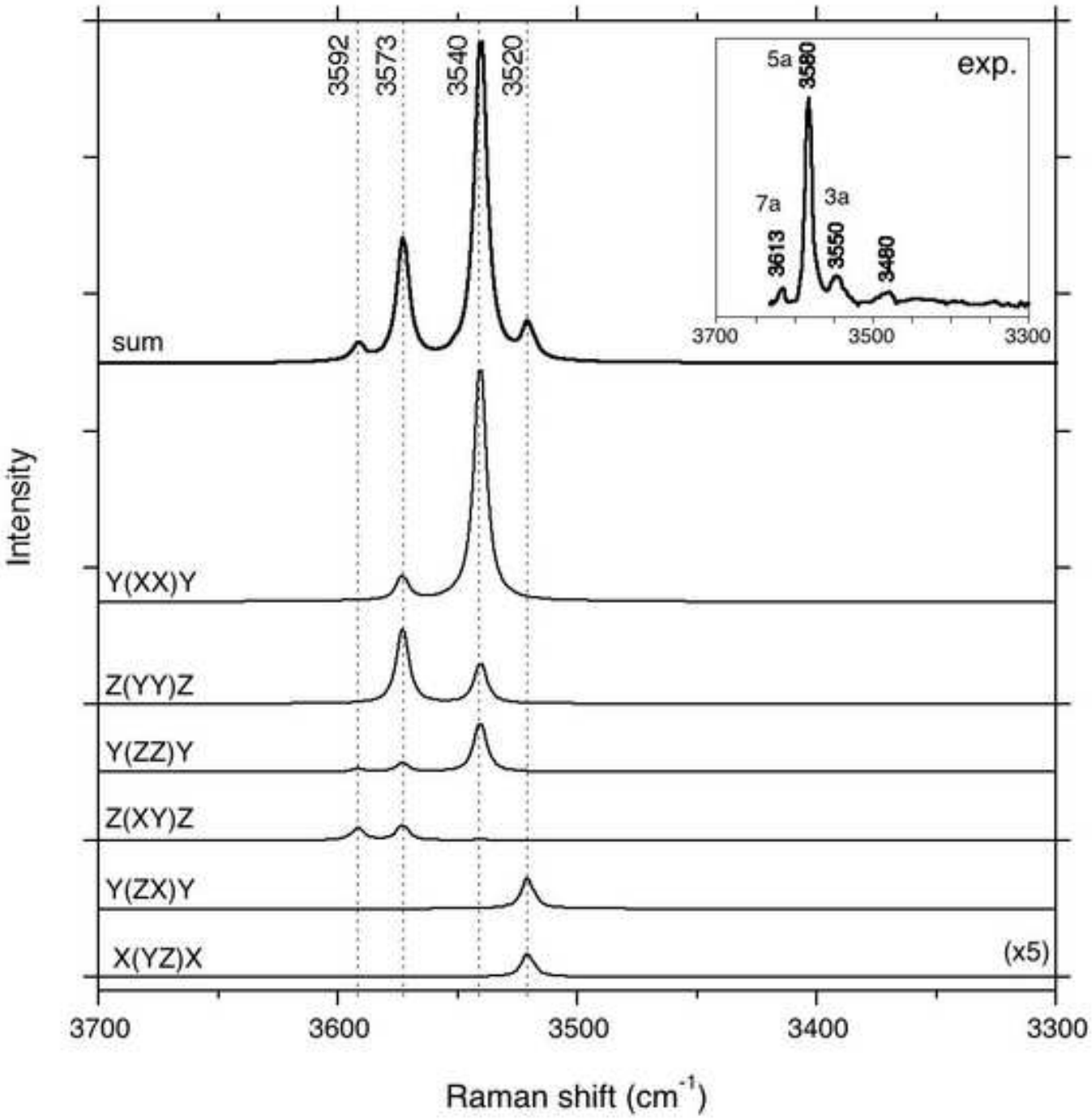

Figure 4

Click here to download Figure Fig4.jpg

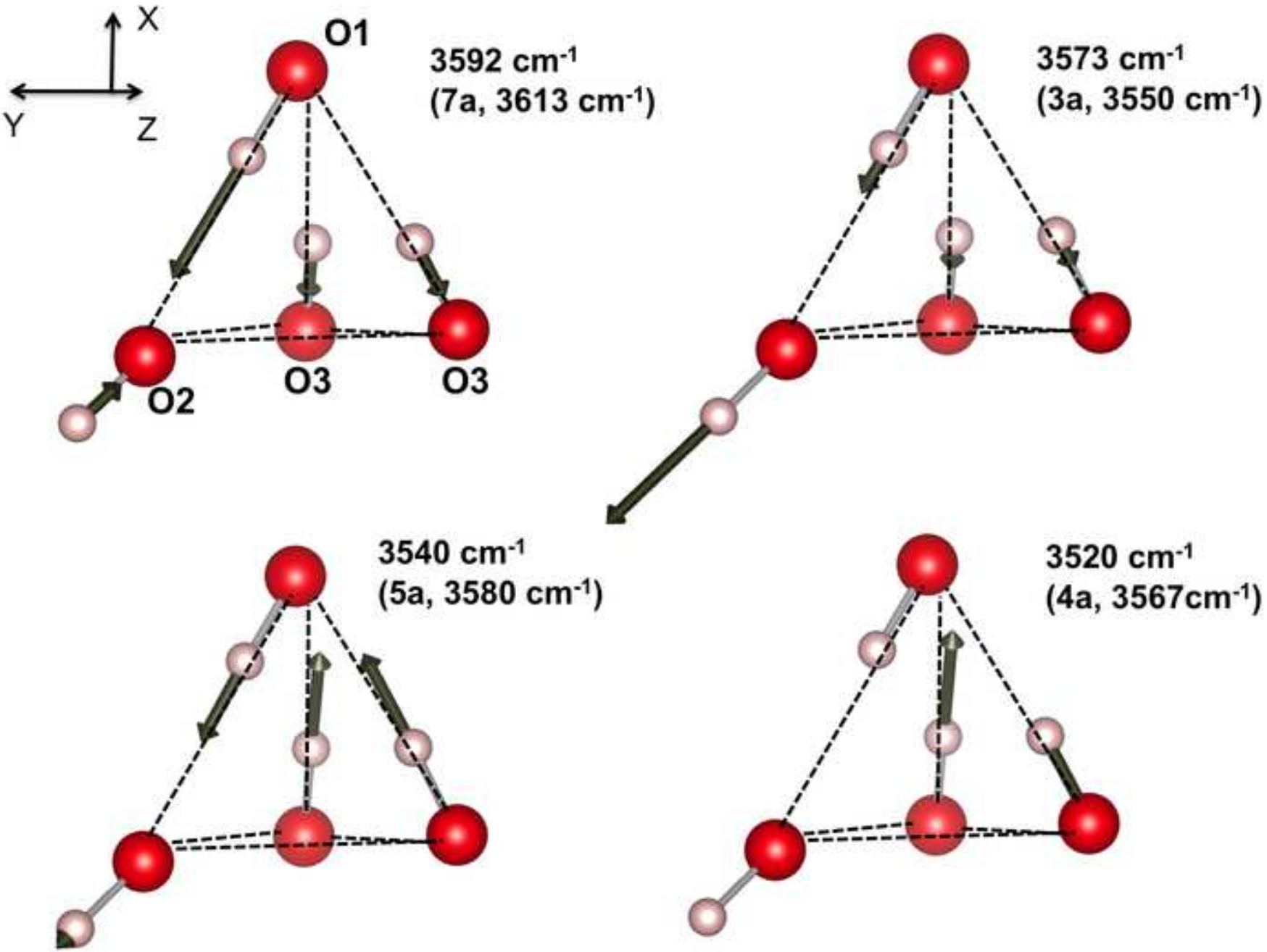

Figure 5

Click here to download Figure Fig5_rev.jpg

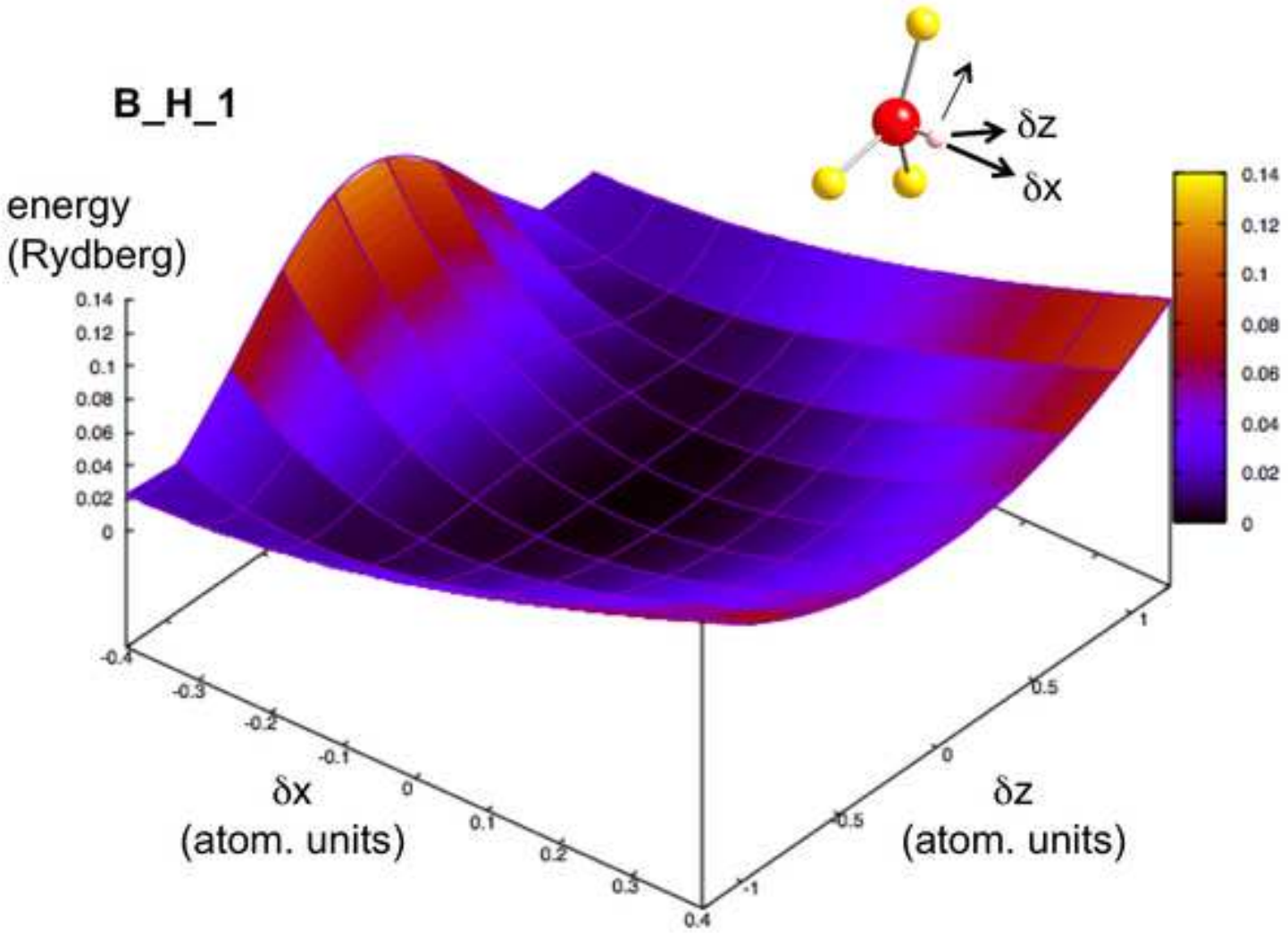

Figure 6

Click here to download Figure Fig6.jpg

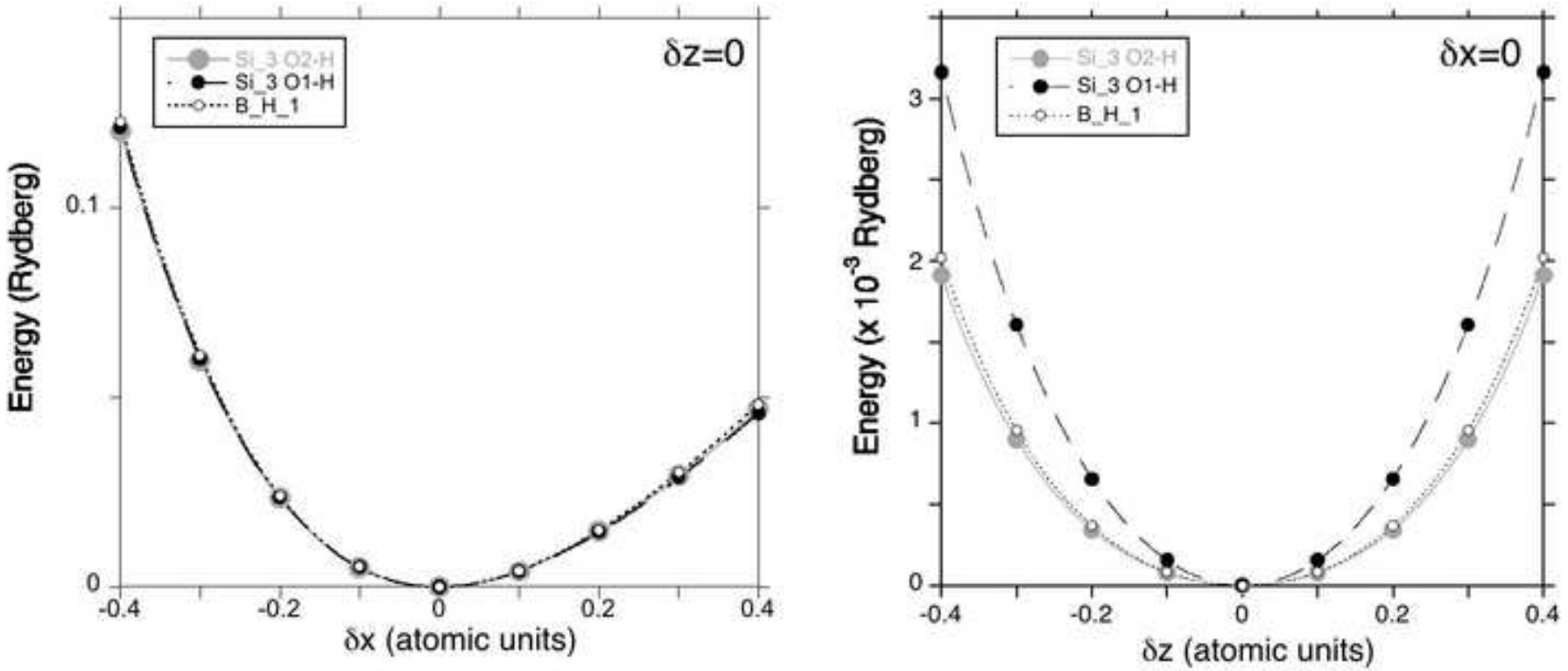

Figure 7

Click here to download Figure Fig7.jpg